Fabrication and Mechanical Properties of Large-Scale Freestanding Nanoparticle Membranes

Jinbo He, Pongsakorn Kanjanaboos, N. Laszlo Frazer, Adam Weis, Xiao-Min Lin, and Heinrich M. Jaeger*

*T*hin-film membranes consisting of nanoparticles are of interest in applications ranging from nanosieves to electric, magnetic, or photonic devices and sensors. However, the fabrication of large-scale membranes in a simple but controlled way has remained a challenge, due to the limited understanding of their mechanical properties. Systematic experiments on ultrathin, freestanding nanoparticle membranes of different core materials, core sizes, and capping ligands are reported. The results demonstrate that a drying-mediated self-assembly process can be used to create close-packed monolayer membranes that span holes tens of micrometers in diameter. Containing up to $\approx 10^7$ particles, these freely suspended layers exhibit remarkable mechanical properties with Young's moduli of the order of several GPa, independent of membrane size. Comparison of three different core–ligand combinations suggests that the membrane's elastic response is set by how tightly the ligands are bound to the particle cores and by the ligand–ligand interactions.

1. Introduction

The ultimate limit of a thin-film membrane is a single layer of atoms. In the form of graphene, the remarkable mechanical properties of such atomically thin, freestanding sheets have recently attracted considerable interest.[1–5] Herein, we investigate their mesoscopic analogue, freestanding monolayers of close-packed nanocrystals or "artificial atoms". These nanocrystal membranes combine several desirable properties.[6–8] They can self-assemble from a solution of ligand-coated nanocrystals in a simple drop-drying process, and they are exceedingly flexible yet strong under indentation, exhibiting Young's moduli of several GPa.[6] The fact that they are hybrid materials composed of inorganic nanocrystal cores surrounded by organic ligand shells allows for unique opportunities to tune their optical and mechanical properties.[7] Furthermore, membranes consisting of particles of different sizes, shapes, and compositions open up new opportunities for use in sensors, nanosieves, or photonic devices.

So far, the available experimental results[6–8] have been confined to membranes based on gold nanoparticles and simulation efforts[9–12] focused on modeling gold cores capped with alkylthiol ligands. Consequently, current understanding of how the mechanical properties depend on the various membrane parameters is still limited. A key outstanding issue concerns the origin of the membranes' ability to sustain large tensile stresses, especially since the ligands typically are short molecules that are liquids at room temperature in bulk. Since van der Waals attractions between the cores alone are too small to account for the tensile stresses,[6,10] the interactions between ligands attached to neighboring cores as well as the core–ligand interactions have to be considered. The effect of varying the ligand size has been investigated through simulations[11,12] and

[*] Prof. H. M. Jaeger, Dr. J. He, P. Kanjanaboos, N. L. Frazer, A. Weis
James Franck Institute and Department of Physics
The University of Chicago
Chicago, IL 60637 (USA)
E-mail: h-jaeger@uchicago.edu

Dr. X.-M. Lin
Center for Nanoscale Materials
Argonne National Laboratory
Argonne, IL 60439 (USA)

⌨ Supporting Information is available on the WWW under http://www.small-journal.com or from the author.

also in recent experiments that used DNA as a tunable ligand,[7] but a direct comparison of the mechanical properties of different core–ligand systems has not been performed.

To shed light on these issues, herein we report a series of experiments on freestanding nanoparticle membranes of different core materials (Au, Fe/Fe$_3$O$_4$, and CoO), different core sizes (mean diameter 5, 13.8, and 8.5 nm, respectively), and different capping ligands (dodecanethiol, oleylamine, and oleic acid, respectively). Our results demonstrate that the drying-mediated assembly process can be adopted for different nanoparticle systems to create close-packed monolayer membranes that span holes of tens of micrometers in diameter. In fact, for CoO we were able to self-assemble membranes over 70-μm-wide square openings, thereby freely suspending ≈10^7 particles. The Young's modulus is found to be of the order of several GPa in all cases, independent of membrane size. Comparison of the three different core–ligand combinations suggests that the membrane strength is set by how tightly the ligands are bound to the particle core and by the ligand–ligand interactions. Finally, we show how the monolayers' mechanical response is modified by adding second and third layers.

2. Results and Discussion

All samples were prepared by depositing a droplet of nanoparticle solution onto a larger water droplet that covered a Si$_3$N$_4$ substrate with prepatterned holes. These holes were created by reactive ion etching (RIE) into 100-nm-thick and 60–70-μm-wide amorphous silicon nitride "window" areas,[13] which allows us to use not only atomic force microscopy (AFM) but also transmission electron microscopy (TEM) to examine the sample both inside and outside the holes. After evaporation of the solvent, the nanoparticles form a compact monolayer at the water/air interface and, as the water slowly evaporates, this monolayer drapes itself over the substrate.[6] Figure 1a–c shows representative AFM and optical images of the resulting freestanding monolayers, self-assembled from Au/dodecanethiol, Fe/Fe$_3$O$_4$/oleylamine, and CoO/oleic acid nanoparticle/ligand combinations and stretched across 5–10-μm-wide holes. Similar to graphene sheets,[2,5] strong van der Waals interactions between the membranes and the substrate not only clamp the membranes down around the hole perimeter, but also pull them into the hole. As can be seen from the AFM images, all membranes recede into the holes by an amount roughly equal to the silicon nitride thickness remaining after the RIE process (confirmed by cross-sectional analysis, see Figure S2 in the Supporting Information) and stretch flat across the hole.

Details of the local membrane structure as well as the particles themselves were examined by TEM after mechanical measurements (Figure 1d–f). The substantial degree of order in the particle arrangements is reflected in the well-defined diffraction patterns (insets of Figure 1d–f). Typical superlattice domain sizes resulting from the fabrication process described
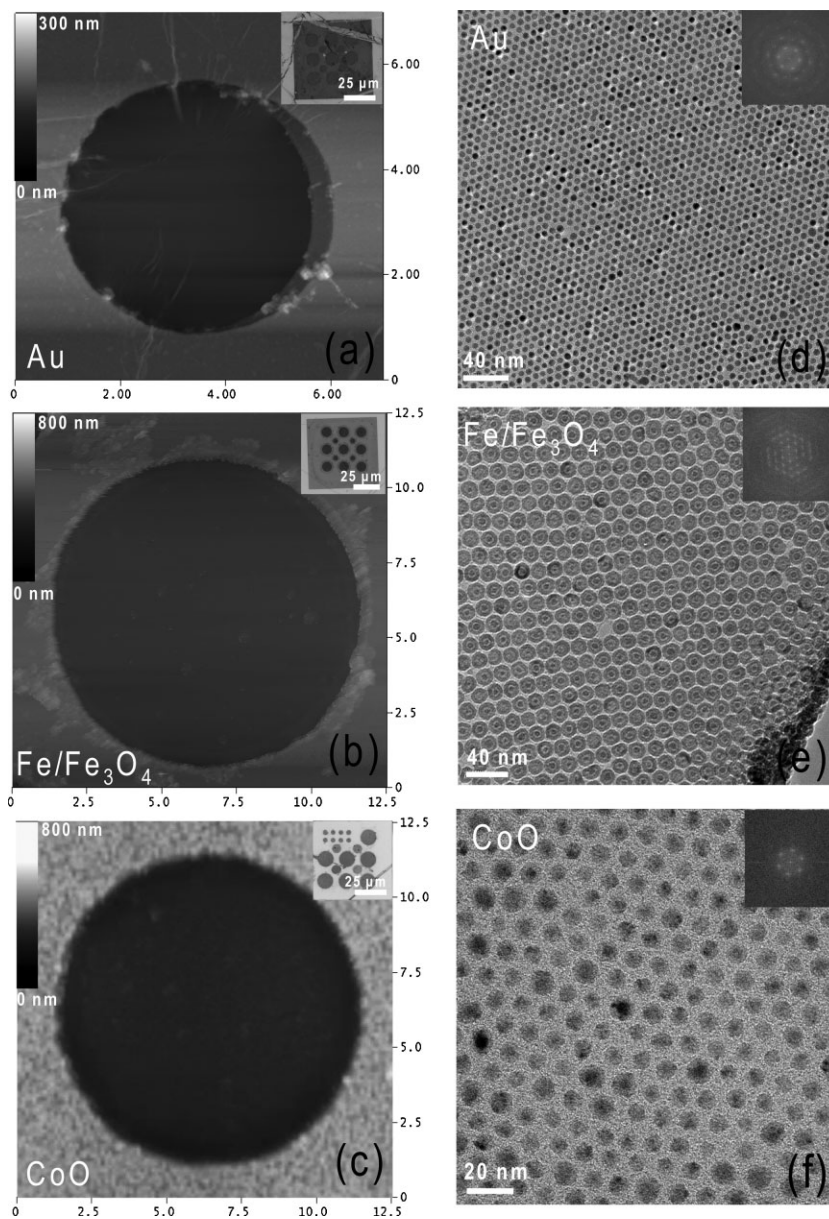
Figure 1. AFM height images (left column) and corresponding TEM details (right column) of monolayer membranes self-assembled from 5 nm Au (a,d), 13.8 nm Fe/Fe$_3$O$_4$ (b,e), and 8.5 nm CoO (c,f) nanoparticles, and stretched across holes 5, 10, and 11 μm in diameter. The steplike feature seen on the right edge of the hole in (a) is an imaging artifact due to the particular shape of the AFM tip used. The iron oxide membrane in (e) was ripped by exposure to the electron beam, similar to the behavior seen in Reference [7]. Left column insets: Optical images of the whole silicon nitride window area with several membranes. Right column insets: Two-dimensional (2D) Fourier transforms of the TEM images.

here are a few hundred nanometers for magnetic Fe/Fe$_3$O$_4$, several micrometers for CoO, and slightly larger for Au. The as-prepared Fe/Fe$_3$O$_4$ nanoparticles are solid core/shell particles; however, continuous oxidation in air creates a seemingly detached yolk/shell morphology, as seen in Figure 1e. CoO nanoparticles are created through gradual oxidation of as-prepared ε-Co nanoparticles in air, through an intermediate stage of Co/CoO core/shell nanoparticles. The average gaps between neighboring particles, measured by TEM, were (1.7 ± 0.3) nm for Fe/Fe$_3$O$_4$ as well as Au, and (2.4 ± 0.6) nm for CoO. Considering the extended lengths of the ligands, ≈1.7 nm for dodecanethiol and ≈2.2 nm for oleylamine and oleic acid, these core–core distances imply that ligand interdigitation is substantial for all the systems investigated. Since the monolayers self-assemble at the liquid/air interface of the drying droplet before they come into contact with the substrate, no difference is expected in the local ordering or the interparticle distances between the freestanding membrane region and adjacent portions of the sheet on the substrate outside a hole. TEM analysis confirms this.

To test the mechanical properties of the membranes, we used AFM to measure the force F required to produce an indentation δ at the center of each membrane. Figure 2a and b shows representative force–indentation curves for the three types of membranes in linear scale and log scale, respectively. For all membranes tested (76 in total), regardless of the type of nanoparticle or membrane diameter, we observed elastic behavior, that is, no significant hysteresis between indentation and retraction of the AFM tip and no noticeable dependence on indentation speed (see also Reference [6]). This differs from the results on much thicker, semiconductor nanoparticle films, for

which viscoelastic behavior was observed.[14] At small indentations, $F(\delta)$ is linear and the slope defines the stiffness of the membrane. From Figure 2a, typical values are of the order of ≈1 N m^{-1}, with CoO membranes being the stiffest. $F(\delta)$ turns nonlinear when δ becomes significantly larger than the film thickness h. Tapping-mode AFM inside the holes reveals well-organized local nanoparticle in-plane arrangements (Figure S3, Supporting Information). The fact that AFM is able to resolve individual particles in the freestanding membrane areas indicates that very little excess ligand remained in the original colloidal solution and no significant excess ligand is deposited directly on top of the membrane, where it could have contributed to the mechanical properties. We therefore take h to be a particle diameter plus two ligand lengths, an estimate also confirmed by direct AFM profilometry of monolayers outside the hole that were scratched to reveal the substrate.

In general, the membrane stiffness is found to decrease with increasing membrane diameter, as long as the samples are prepared and tested in the same set of experiments.[6] Also, increasing ligand length has been found to reduce stiffness.[7] However, since the stiffness is greatly affected by any prestrain that might arise during the draping and drying, comparison of the slopes of force curves in different experimental runs that use different materials can only give a rough, qualitative indication of relative strengths. For quantitative comparison, a more detailed analysis is required that extracts the Young's modulus.

To this end, a very useful and straightforward approach for two-dimensional (2D) sheets was recently introduced by Lee and co-workers,[5] who tested its validity by comparing experimental results on monolayer graphene with extensive simulations. To excellent approximation, for an indented, 2D elastic disk clamped along its circumference the contributions from prestrain and stretching add linearly so that $F(\delta)$ can be written as:[5]

$$F = \sigma^{2D}(\pi R)\left(\frac{\delta}{R}\right) + E^{2D}\left(q^3 R\right)\left(\frac{\delta}{R}\right)^3 \qquad (1)$$

Here, R is the radius of the membrane, $q = (1.05 - 0.15\nu - 0.16\nu^2)^{-1}$ is a constant that depends on the Poisson ratio ν ($\nu = 1/3$ and $q = 1.02$ in our case), σ^{2D} is the prestress, and E^{2D} is the elastic constant of the 2D disk. The 2D approximation is valid as long as any bending stiffness can be neglected, that is, for systems where $R/h > 1$. For our 10-μm-diameter membranes, $R/h > 500$. To check the effects of AFM tip placement and tip radius r on $F(\delta)$, we performed simulations of 2D ball–spring networks mimicking the experiments. We found that both can be neglected as long as the tip contacts the membrane within $R/3$ of its center and $r/R \ll 1$ (confirmed by scanning electron microscopy (SEM) analysis of the AFM tips). In the limit of large indentations,
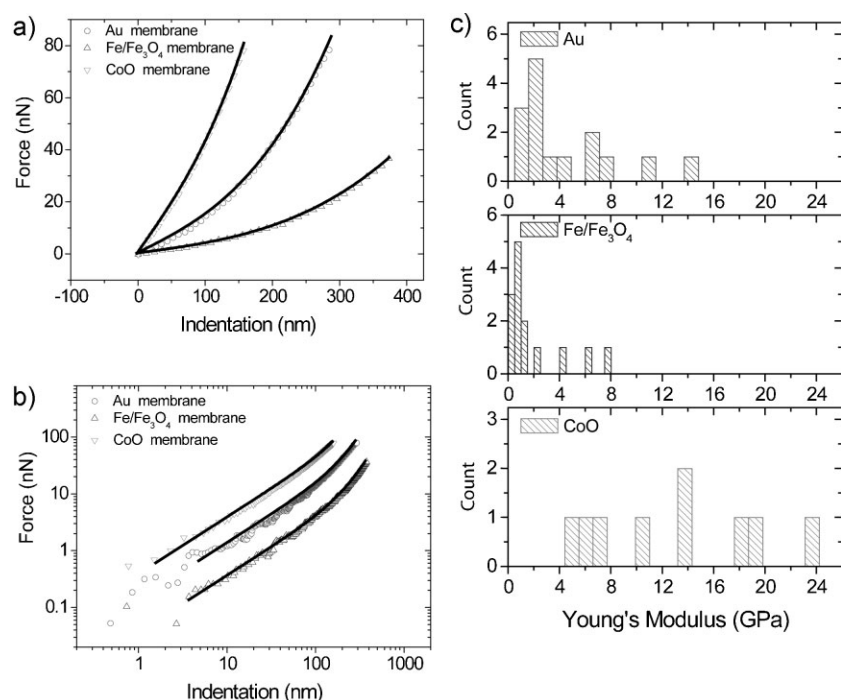
Figure 2. a) Representative force–indentation curves for Au, Fe/Fe$_3$O$_4$, and CoO nanoparticle monolayer membranes of diameter 10 μm. The black lines represent fits to Equation (1). b) Log–log plot of the data in (a). c) Histograms of Young's moduli E obtained from fits to Equation (1).

Equation (1) approaches the prestress-independent asymptote $F = q^3 (ERh)(\delta/R)^3$ for stretched elastic sheets, where $E = E^{2D}/h$ is the Young's modulus. As long as the indentation is deep enough to produce some nonlinearity, fits of $F(\delta)$ to Equation (1) therefore allow us to extract both the prestrain, given by σ^{2D}/E^{2D}, and the Young's modulus E.

Figure 2c shows histograms of the Young's moduli determined in this way. The average values are found to be ≈ 1 GPa for Fe/Fe$_3$O$_4$, ≈ 4 GPa for Au, and ≈ 14 GPa for CoO (E for Au is 30% smaller than previously reported in Reference [6], but the current value is more reliable because it is obtained from fits to the full trace of $F(\delta)$ and not just from the large-F asymptote). Within the scatter of the measurements, no obvious trend in the dependence of the Young's moduli on the membrane diameter is observed (Figure S4a, Supporting Information), and similarly there is no obvious correlation between Young's modulus and prestrain (Figure S4b, Supporting Information). It is likely that the observed spread in Young's moduli is caused to a large degree by defects in the local, close-packed particle arrangements, but in this work we have not tracked and analyzed those defects. The concentration of data points at the lower-left corner of Figure S4b–d (Supporting Information) is due to the fact that it is experimentally difficult to extract E from monolayers with large prestrain, because $F(\delta)$ in this case is predominantly linear over the accessible experimental range and therefore no reliable fitting to the second term in Equation (1) can be carried out.

The large intrinsic strength of CoO membranes allows them to stretch across holes significantly bigger than 10 μm. Using ethylene glycol instead of water as the hydrophilic droplet and performing the drying at 100–130 °C under either argon or ambient conditions, CoO membranes covering up to 70 μm could be prepared. Figure 3a shows a low-resolution TEM image of a 70×70 μm^2 freestanding membrane. The visible wrinkles at the four corners provide a direct hint of the elastic properties of the sheet and of the prestrain introduced during drying. At higher resolution, TEM confirms that this membrane consists of a single layer of CoO particles (Figure 3b), although these particles are more oxidized and less ordered than in Figure 1f. Based on the average particle spacing, we estimate that over 10 million CoO nanoparticles are present in this membrane. The hysteresis at very large indentations (>1 μm) in $F(\delta)$ for this membrane (Figure 3c) can be attributed to the membrane adhering onto the side of the large and blunt plateau-type AFM tip used in this measurement (see Figure S5, Supporting Information). From fits to $F(\delta)$ a value $E \approx 13.6$ GPa is obtained, close to the average Young's modulus of smaller CoO membranes (Figure 2b), thus confirming

that the strength remains unchanged even for extended membranes.

To address the possible causes for the different mechanical properties of the three systems investigated, we consider two neighboring nanoparticles and their interdigitating ligand shells, as shown in Figure 3d. Ligands, which stabilize the particles and prevent the cores from sintering, are typically attached to the particle surfaces through coordination bonds. Interdigitating ligands attract each other by van der Waals forces, thereby providing mechanical connectivity. Since the particle cores are metals or metal oxides, which have much larger Young's moduli ($E_{\text{gold}} \cong 78$ GPa, $E_{\text{cobalt}} \cong 209$ GPa, $E_{\text{iron oxide}} \cong 350$ GPa) than the measured E values, the elastic properties of the nanoparticle membranes are dominated by the ligand–core and ligand–ligand interactions.

It is well known that dodecanethiol chemically absorbed onto flat Au surfaces through Au–S coordination bonds assembles into a crystalline state.[15–17] For nanoparticle surfaces with their intrinsically high curvature and limited size of crystalline facets, the ordering of the ligands is expected to be reduced.[17] Nevertheless, comparison of the Fourier transform infrared (FTIR) spectra of pure dodecanethiol in the liquid state and dodecanethiol-covered Au nanoparticles (Figure 4a) suggests that the ligands on the gold-nanoparticle surfaces show some ordering, as indicated by the red shift of the asymmetric CH$_2$ stretch from 2923 to 2917 cm^{-1} in our sample due to the increased ligand density (a factor of between 1 and 2 for gold).[17] In addition, the remaining sharp peak at 1466 cm^{-1},
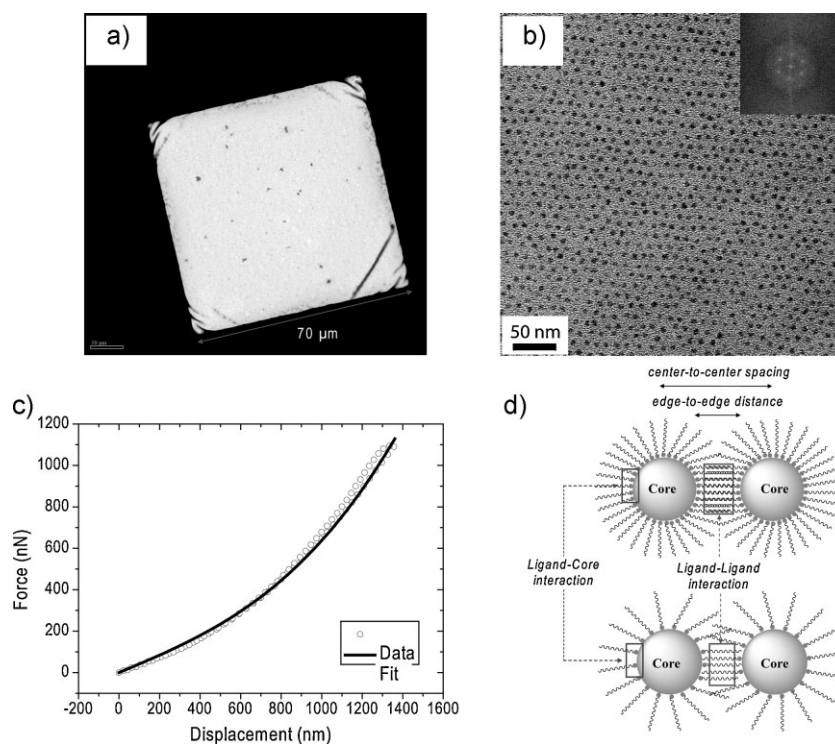
**Figure 3.** a) TEM image of a 70×70 μm^2 freestanding membrane consisting of a monolayer of CoO particles. b) Higher-resolution TEM detail of the image in (a). Inset: the corresponding Fourier transform. c) Force–indentation curve taken with a blunt plateau tip (see Figure S5, Supporting Information). The black line represents the fitting curve using Equation (1). d) Schematic view of two interdigitated nanoparticles.

attributed to the scissoring motion of an all-*trans* methylene chain, along with a series of sharp peaks ranging from 1000 to 1400 cm^{-1}, indicate a high surface density and good packing geometry of dodecanethiol ligands on nanoparticle surfaces.[17]

FTIR experiments were also carried out to identify the ligands status of oleic acid and oleylamine on the nanoparticle surfaces in our study. The FTIR data of pure oleic acid and oleic acid-covered CoO nanoparticles are shown in Figure 4b. The 1710 cm^{-1} peak (C=O stretching), which is present in the IR

spectrum of the pure oleic acid, disappeared for the nanoparticles, which indicates complete chemisorption of oleic acid onto the CoO surface.[18] Two new peaks at 1546 (weak) and 1404 cm^{-1} (strong) represent the asymmetric and symmetric COO$^-$ stretch, which suggests that the ligand coverage on the particle surface is high, and that the interaction between the carboxylate head group and the cobalt atom is bridging bidentate, that is, two oxygen atoms in the carboxylate group coordinate symmetrically with different Co atoms.[19] In addition, a red shift of the features associated with CH$_2$ asymmetric ($\approx$2920 cm^{-1}) and symmetric stretching ($\approx$2850 cm^{-1}) was observed, which indicated that the ligands on particle surfaces form a more ordered state.[18] The FTIR data for pure oleylamine and oleylamine-covered Fe/Fe$_3$O$_4$ nanoparticles are shown in Figure 4c. The spectrum shows that there is very little red shift of the asymmetric CH$_2$ stretch, similar to the recently published FTIR spectra for oleylamine on similar particles, which suggests that this ligand lacks good packing geometry on Fe$_3$O$_4$ surfaces.[20] In addition, the significant broadening of peaks in the region from 1300 to 1500 cm^{-1} indicates a low ligand density on the Fe$_3$O$_4$ shell.

Direct TEM analysis also supports our conclusion that the ligand packing density on the three particle types is significantly different. The average gap between neighboring nanoparticles observed from TEM is (1.7 ± 0.3) nm for gold and iron oxide, and (2.4 ± 0.6) nm for cobalt oxide. The length of free dodecanethiol is close to 1.7 nm and for oleyamine and oleic acid it is close to 2.2 nm. Therefore, for Au and CoO, the ligand shells are fully interdigitated with the gap between nanoparticles being close to a single molecule's length. By contrast, in the Fe/Fe$_3$O$_4$ system the ligand packing density is lower, which allows molecules to bend and the interparticle gap to be significantly smaller than the length of individual molecules.[21] We also noticed that during the nanoparticle preparation, Fe/Fe$_3$O$_4$ nanoparticles cannot withstand extensive washing processes and are prone to aggregation, which means oleylamine does not bind to the nanoparticle surface strongly, unlike dodecanethiol ligands for Au and oleic acid for CoO
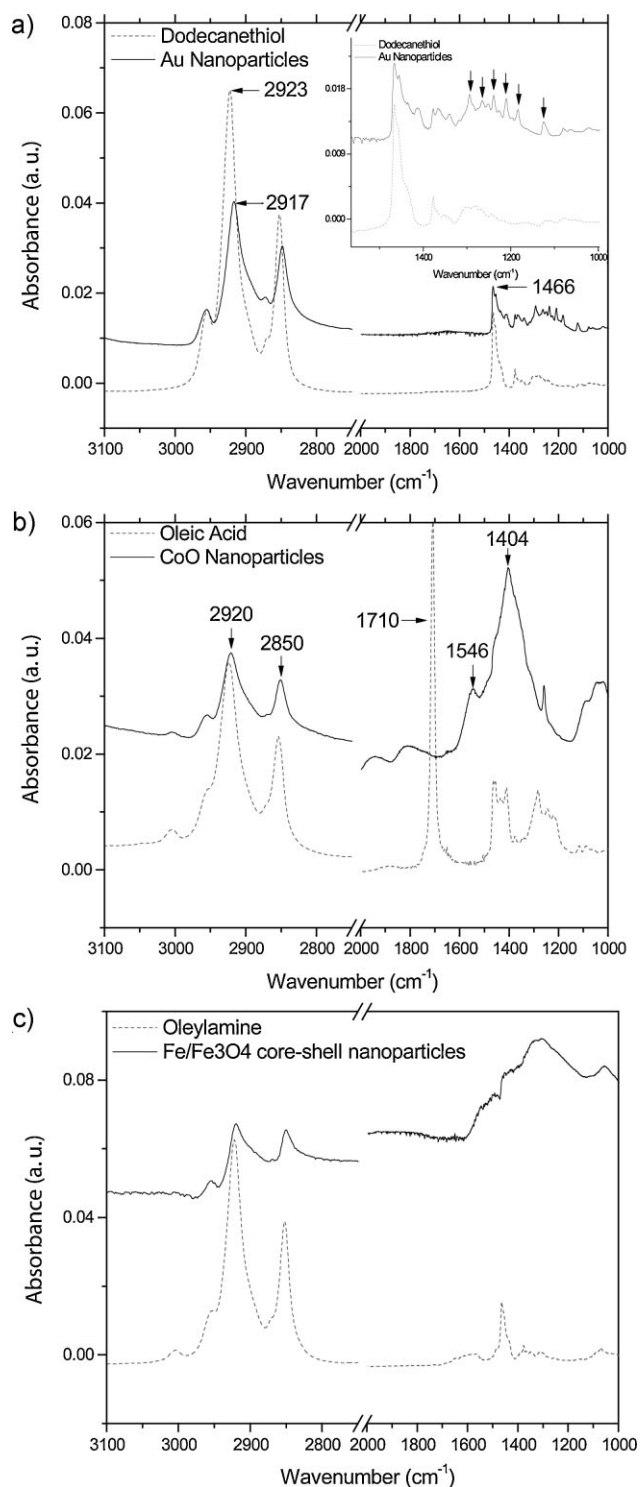
Figure 4. a) FTIR data of pure dodecanethiol and dodecanethiol-covered Au nanoparticles. The asymmetric CH$_2$ stretch shifted from 2923 to 2917 cm^{-1}. The remaining sharp peak at 1466 cm^{-1}, attributed to the scissoring motion of an all-*trans* methylene chain, along with a series of sharp peaks ranging from 1000 to 1400 cm^{-1} indicate a high surface density and good packing geometry of dodecanethiol ligands on nanoparticle surfaces. b) FTIR data of pure oleic acid and oleic acid-covered CoO nanoparticles. A red shift of the features associated with CH$_2$ asymmetric ($\approx$2920 cm^{-1}) and symmetric stretching ($\approx$2850 cm^{-1}) indicates that the ligands on the particle surfaces form a more ordered state. The absence of the 1710 cm^{-1} peak for CoO nanoparticles, which is attributed to C=O stretching, indicates complete chemisorption of oleic acid onto the CoO surface. Two new peaks at 1546 (weak) and 1404 cm^{-1} (strong) represent the asymmetric and symmetric COO$^-$ stretch, respectively, which suggests that the ligand coverage on the particle surface is high, and that the interaction between the carboxylate head group and the cobalt atom is bridging bidentate. c) FTIR data of pure oleylamine and oleylamine-covered Fe/Fe$_3$O$_4$ nanoparticles. The spectrum shows that there is very little red shift of the asymmetric CH$_2$ stretch, which suggests that this ligand lacks good packing geometry on the Fe$_3$O$_4$ surface. The significant broadening of peaks in the region from 1300 to 1500 cm^{-1} indicates a low ligand density on the Fe$_3$O$_4$ shell.

nanoparticles. This finding is also consistent with another published report.[22] These observations clearly indicate that the oleylamine–Fe$_3$O$_4$ interaction is weaker than in the other two cases.

As the ligand–core interaction increases, the ligand density on the nanoparticle surface increases, which results in a better packing geometry of the ligands and increased interdigitated and oriented CH$_2$ groups per chain between two neighboring nanoparticles, as sketched in Figure 3d. With the resulting, larger volume fraction of better-packed ligands, the net energy needed to break the bonds is enhanced, which is confirmed by the observed increase of the ligand melting temperature in the confined geometry,[6] as well as the strong mechanical resilience of the membrane observed in this work. This behavior is similar to the results reported for short alkyl chain[23,24] and larger alkyl chain materials such as polyethylene.[25,26] As the length of the alkyl chain increases, the possibility of interdigitation is increased due to the decreased volume fraction of defects caused by the CH$_3$ end group,[23,24] which should increase the melting temperature and mechanical properties as well. Another conclusion is that, as the particle core size increases slightly and thus the curvature of the particle surface is lowered, the local density of interdigitated ligands between the nanoparticles will be enhanced, which will promote stronger interactions between ligands. The net effect is that the membrane's mechanical stiffness is expected to increase.

According to the analysis above, since the interaction between CoO and oleic acid is strong and the ligand length is large (2.2 nm), CoO membranes are expected to be the stiffest among the three. The interaction between gold and thiol is strong but the length of dodecanethiol (1.7 nm) is shorter than that of oleic acid and the core size of gold is smaller than that of CoO. It is therefore reasonable that gold membranes are somewhat weaker than CoO membranes. The interaction between iron oxide and oleylamine is the weakest. Even though it has the same ligand length as oleic acid and the largest core size of these three, the low ligand density on the surface causes less interdigitation between adjacent nanoparticles, which finally results in the smallest Young's modulus. This result also suggests that, in the alkyl-chain ligated system, the ligand–core interaction is the dominating factor for the mechanical properties. On the other hand, for a given ligand–core interaction, ligand length and core size will also affect the mechanical properties by changing the ligand–ligand interaction.

Based on the explanation provided above, it is reasonable to speculate that the intrinsic strength of the nanoparticle membranes will be determined by the weaker of the ligand–core and ligand–ligand interactions. In the alkyl-chain ligated nanoparticle system, the bond energy for interdigitated alkyl chains is much lower than the ligand–core bond energy.[23] In this case, the ligand–ligand interaction determines the intrinsic strength of the membrane. However, as stronger ligand–ligand interactions are introduced, for example strong hydrogen bonding between DNA molecules, the ligand–core interaction could become the weak link.

By increasing the nanoparticle concentration and not letting the solution drain from the chip surface, multilayers can be produced. Figure 5 compares the force–indentation curves
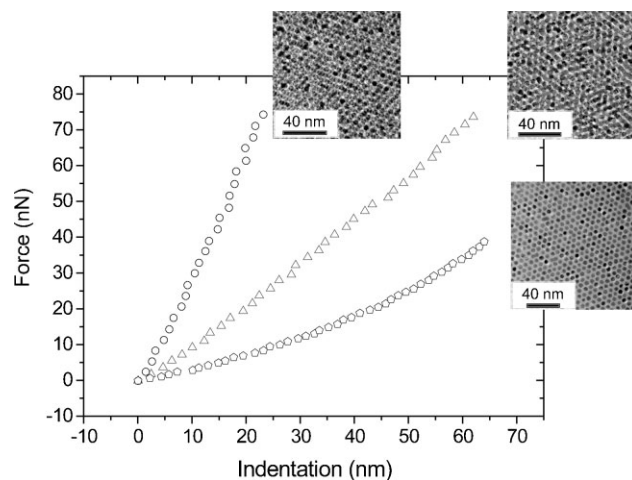
Figure 5. Force versus indentation curves of one (pentagon)-, two (triangle)-, and three (circle)-layer-thick Au nanoparticle membranes, all stretched across 2-μm-diameter holes. Insets: TEM detail images of the corresponding membranes.

for one (pentagon)-, two (triangle)-, and three (circle)-layer-thick gold membranes stretched across 2-μm holes. The insets give the TEM details. The double- and triple-layer membranes recede into the holes just as the monolayers do. The force–indentation curves show an enhanced stiffness (by factors of ≈3 and 8, respectively) and a much more linear behavior than the monolayer. This extended linear response might be produced by an enhanced prestrain during the drying process. Alternatively, it could arise from contributions to the bending energy, which does not play a significant role for monolayers but will become important as the membrane gets thicker. These double- and triple-layer membranes simply break at larger forces, well before significant nonlinearities set in, and therefore Young's moduli could not be deduced.

3. Conclusions

In summary, we have demonstrated a one-step drying process to create large-scale freestanding ultrathin monolayers of different core materials, sizes, and ligands. The experimental results show that 1) the Young's moduli of the nanoparticle membranes do not vary with the size of the membranes, 2) the membrane gets stiffer as the thickness increases, and 3) the mechanical properties depend on both the ligand–core and ligand–ligand interactions. Based on the mechanical properties of three kinds of membranes, we conclude that, at least for our particle sizes, the core–ligand strength of iron oxide–oleylamine is weaker than the cobalt–oleic acid and gold–dodecanethiol interaction. The ability to produce robust membranes that are as thin as a single layer of close-packed nanocrystals but extend freely over tens of micrometers, while exhibiting effective Young's moduli in the GPa range, should make these ultrathin films suitable for a range of applications, including resonators or nanoporous filters. In particular, these hybrid systems offer unique opportunities to combine the intrinsic optical, electrical, or magnetic properties of nanoparticles with different functionalities of the ligands.[27,28]

4. Experimental Section

Nanoparticle synthesis: Au nanoparticles were synthesized by reducing Au salt with sodium borohydride in an inverse micelle solution, followed by a digestive ripening process using an excess amount of dodecanethiol ligand to narrow the particle size.[29] TEM analysis of the samples showed average diameters of ≈5 nm with size dispersion <10%. Fe nanoparticles were synthesized by thermal decomposition of $Fe(CO)_5$ at 180 °C in the presence of oleylamine, according to the procedure developed by Peng et al.[30] Subsequent treatment with $(CH_3)_3NO$ for 20 min at 240 °C yielded Fe/Fe_3O_4 core/shell nanoparticles. TEM of as-prepared samples showed a 2.5-nm-thick oxide shell grown directly on the 8.8-nm-diameter Fe core. As the samples were further processed in air, a seemingly visible gap developed between the initial oxide shell and the interior Fe core (visible in the TEM images in Figure 1). ε-Co nanoparticles were obtained through thermal decomposition of $Co_2(CO)_8$ in dichlorobenzene with oleic acid and small amounts of trioctylphosphine oxide (TOPO) as ligand.[31] Subsequent exposure to air caused complete oxidation to CoO, as confirmed by X-ray diffraction. TEM studies showed CoO nanoparticles with an average diameter of ≈8.5 nm.

Sample fabrication: Silicon wafer chips (3×4 mm^2) coated with 100–120 nm silicon nitride were used as substrates. At two spots near the center of each chip, the silicon was etched away from the rear to create square, TEM-transparent silicon nitride "window" areas ≈70 μm along the side. Circular holes with diameters ≈2, ≈5, and 11–13 μm were fabricated into the window areas by electron-beam lithography and RIE (see Supporting Information, Figure S1a). Membrane preparation followed the procedure published in our previous work.[6] Briefly, as indicated in Figure S1b (Supporting Information), silicon nitride chips were placed on a clean glass slide or a piece of Teflon tape. A water droplet (8 μL) was placed onto the chip, and then nanoparticle solution (20 μL) was applied on top of the water. Due to the low surface tension of the solvent (usually toluene), the nanoparticle solution expanded and quickly covered the water droplet. After the solvent (toluene) evaporated (in several minutes), a monolayer of nanoparticles was left at the water/air interface. The substrate with the water drop was then lifted onto a mesh to dry and, as the water receded, the nanoparticle membranes draped themselves across the holes in the substrate. A total of ≈125 membranes were fabricated. The success rates for the preparation of large-scale (>5 μm) Au, Fe/Fe_3O_4, and CoO membranes were 50, 50, and 80%, respectively (for smaller hole sizes the success rates were higher). All three kinds of membranes showed wrinkles and folds during preparation. Fe/Fe_3O_4 membranes usually had smaller-scale (<100 nm in width) wrinkles or folds than Au and CoO membranes. All large-scale membranes were sensitive to the electron beam. High-intensity beams could damage the membranes (see Figure 1e and Reference [7]) and for this reason all AFM measurements were performed before TEM analysis.

AFM: Veeco Nanoscope III and Asylum MFP-3D AFM instruments were used for imaging in the tapping mode as well as for extracting force–indentation curves in the contact mode. Force-modulation silicon cantilevers were used with average spring constants of ≈1 N m^{-1} (Olympus AC240) and ≈3 N m^{-1} (Budget Sensor Multi75DLC). The exact spring constant for each tip was determined to better than 10% with the Asylum MFP-3D apparatus using its thermal spectrum mode. The typical tip speed for the indentation was 500 nm s^{-1} with a repeating frequency of 0.5 Hz. Each nanoparticle membrane was first imaged by AFM, then indented tens of times to collect the force–indentation curve, and finally imaged again to check for damage. For large cobalt membranes, plateau tips (Nanosensors PL2-FMR-SPL) with a cylindrical tip head (diameter ≈1.8 μm, average spring constant ≈1.5 N m^{-1}) were used.

Optical microscopy, TEM, and SEM: TEM imaging of each sample was conducted with a Tecnai F30 microscope at 300 kV. This was done after AFM force measurements to prevent electron-beam-induced crosslinking of the ligands. Optical images were taken with an Olympus BH-2 microscope with attached Olympus DP72 CCD camera.

FTIR spectroscopy: FTIR experiments were conducted using a Bruker Vertex 70 spectrometer and Pike "MiRacle" attenuated total reflectance (ATR) accessory with single-reflection Ge crystal. Au and CoO nanoparticles were precipitated and washed with ethanol once, and Fe/Fe_3O_4 nanoparticles were precipitated and washed with butanol once. After drying the precipitate in a vacuum, powder was deposited on the ATR crystal and spectra were measured from 650 to 4000 cm^{-1} with 1 cm^{-1} resolution.

[1] J. S. Bunch, A. M. van der Zande, S. S. Verbridge, I. W. Frank, D. M. Tanenbaum, J. M. Parpia, H. G. Craighead, P. L. McEuen, *Science* **2007**, *315*, 490–493.

[2] J. S. Bunch, S. S. Verbridge, J. S. Alden, A. M. van der Zande, J. M. Parpia, H. G. Craighead, P. L. McEuen, *Nano Lett.* **2008**, *8*, 2458–2462.

[3] I. W. Frank, D. M. Tanenbaum, A. M. Van der Zande, P. L. McEuen, *J. Vac. Sci. Technol. B* **2007**, *25*, 2558–2561.

[4] C. Gomez-Navarro, M. Burghard, K. Kern, *Nano Lett.* **2008**, *8*, 2045–2049.

[5] C. Lee, X. D. Wei, J. W. Kysar, J. Hone, *Science* **2008**, *321*, 385–388.

[6] K. E. Mueggenburg, X. M. Lin, R. H. Goldsmith, H. M. Jaeger, *Nat. Mater.* **2007**, *6*, 656–660.

[7] W. L. Cheng, M. J. Campolongo, J. J. Cha, S. J. Tan, C. C. Umbach, D. A. Muller, D. Luo, *Nat. Mater.* **2009**, *8*, 519–525.

[8] H. Xia, D. Wang, *Adv. Mater.* **2008**, *20*, 4253–4256.

[9] W. D. Luedtke, U. Landman, *J. Phys. Chem.* **1996**, *100*, 13323–13329.

[10] W. D. Luedtke, U. Landman, *J. Chem. Phys. B* **1998**, *102*, 6566–6572.

[11] P. Schapotschnikow, R. Pool, T. J. H. Vlugt, *Nano Lett.* **2008**, *8*, 2930–2934.

[12] U. Landman, W. D. Luedtke, *Faraday Discuss.* **2004**, *125*, 1–22.

[13] T. L. Morkved, W. A. Lopes, J. Hahm, S. J. Sibener, H. M. Jaeger, *Polymer* **1998**, *39*, 3871–3875.

[14] D. Lee, S. G. Jia, S. Banerjee, J. Bevk, I. P. Herman, J. W. Kysar, *Phys. Rev. Lett.* **2007**, *98*, 026103(1–4).

[15] A. Ulman, *Chem. Rev.* **1996**, *96*, 1533–1554.

[16] J. C. Love, L. A. Estroff, J. K. Kriebel, R. G. Nuzzo, G. M. Whitesides, *Chem. Rev.* **2005**, *105*, 1103–1169.

[17] M. J. Hostetler, J. J. Stokes, R. W. Murray, *Langmuir* **1996**, *12*, 3604–3612.

[18] N. Q. Wu, L. Fu, M. Su, M. Aslam, K. C. Wong, V. P. David, *Nano Lett.* **2004**, *4*, 383–386.

[19] P. Dallas, A. B. Bourlinos, D. Niarchos, D. Petridis, *J. Mater. Sci.* **2007**, *42*, 4996–5002.

[20] Z. C. Xu, C. M. Shen, Y. L. Hou, H. J. Gao, S. S. Sun, *Chem. Mater.* **2009**, *21*, 1778–1780.

[21] X. M. Lin, R. Parthasarathy, H. M. Jaeger, in *Encyclopedia of Nanoscience and Nanotechnology* (Eds: J. A. Schwarz, C. Contescu, K. Putyera), Marcel Dekker, New York **2004**, p. 2245.

[22] M. Klokkenburg, J. Hilhorst, B. H. Erne, *Vib. Spectrosc.* **2007**, *43*, 243–248.

[23] J. Watanabe, H. Ono, I. Uematsu, A. Abe, *Macromolecules* **1985**, *18*, 2141–2148.

[24] R. H. Terrill, T. A. Postlethwaite, C. H. Chen, C. D. Poon, A. Terzis, A. D. Chen, J. E. Hutchison, M. R. Clark, G. Wignall, J. D. Londono, R. Superfine, M. Falvo, C. S. Johnson, E. T. Samulski, R. W. Murray, *J. Am. Chem. Soc.* **1995**, *117*, 12537–12548.

[25] M. Matsuo, C. Sawatari, *Macromolecules* **1986**, *19*, 2036–2040.

[26] C. Sawatari, M. Matsuo, *Macromolecules* **1986**, *19*, 2726–2732.

[27] G. Hodes, *Adv. Mater.* **2007**, *19*, 639–655.

[28] C. Y. Jiang, V. V. Tsukruk, *Adv. Mater.* **2006**, *18*, 829–840.

[29] X. M. Lin, H. M. Jaeger, C. M. Sorensen, K. J. Klabunde, *J. Phys. Chem. B* **2001**, *105*, 3353–3357.

[30] S. Peng, C. Wang, J. Xie, S. H. Sun, *J. Am. Chem. Soc.* **2006**, *128*, 10676–10677.

[31] A. C. S. Samia, K. Hyzer, J. A. Schlueter, C. J. Qin, J. S. Jiang, S. D. Bader, X. M. Lin, *J. Am. Chem. Soc.* **2005**, *127*, 4126–4127.